analytical chemistry

pubs.acs.org/ac Article

Metal Defect-Mediated Adsorption-Catalytic Platform Drives Efficient Electrochemiluminescence Sensing

Yamei Li, Xue Dong, Yujie Han, Rui Feng,* Yu Du,* Huangxian Ju, and Qin Wei*

Cite This: *Anal. Chem.* 2026, 98, 6139−6148 Read Online

ACCESS | Metrics & More | Article Recommendations | Supporting Information

ABSTRACT: The rational design of highly active catalytic interfaces is of crucial importance for the construction of sensitive and reliable electrochemiluminescence (ECL) biosensors. In this study, a metal defect-mediated adsorption-catalytic interface, specifically La-deficient $LaCoO_3$ (LCO-V_{La}), was rationally constructed via a cation vacancy engineering strategy. The introduction of La vacancy (V_{La}) significantly enhanced the adsorption capacity for the coreactant ($K_2S_2O_8$) and concurrently exposed more Co-rich active surfaces. The multivalent redox reversible reaction of Co facilitated an increase in the bond length of the O−O bond in $S_2O_8^{2-}$ from 1.48 to 1.54 Å, which made the O−O bond easier to break, thus significantly improving the interfacial catalytic activity. The dual ligands endowed the framework with excellent electroluminescent properties and chemical stability. The porphyrin groups coordinated at the center of the framework extended the π-conjugation length, which in turn enhanced the charge mobility and ECL efficiency of the emitter. Herein, the synergistic effect between the metal defect-mediated adsorption-catalytic interface and the dual-ligand framework structure enhanced the ECL signal, enabling the highly sensitive detection of microcystin-LR (MC-LR). The sensing strategy provides a reliable analytical tool for the quantitative analysis and online monitoring of ultratrace pollutants in complex environmental matrices.

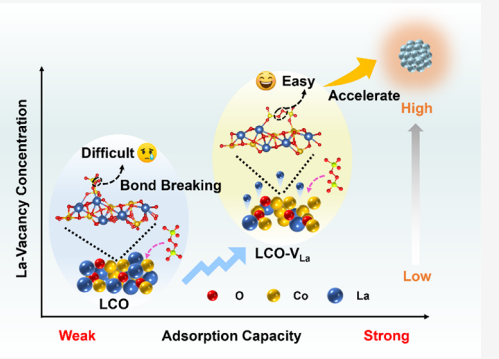

INTRODUCTION

Microcystin-LR (MC-LR), a representative cyclic heptapeptide toxin released during cyanobacterial blooms, possesses a unique Adda side chain that confers potent protein phosphatase inhibition, subsequently eliciting hepatocellular injury and potential liver carcinogenesis.[1,2] Owing to its ubiquity globally in aquatic environments, the emergence of highly sensitive methods for trace MC-LR determination has become a central challenge in environmental analytical chemistry.[3] In recent years, techniques such as high-performance liquid chromatography−mass spectrometry, enzyme-linked immunosorbent assay, and electrochemical sensing have been widely applied for the detection of MC-LR.[4−6] These methods, however, exhibit drawbacks, including expensive instrumentation, time-consuming pretreatment procedures, poor electrode stability, and insufficient sensitivity for trace analysis requirements.[4,7] Therefore, it is urgent to develop a new method with high sensitivity and stability to achieve accurate monitoring of MC-LR.

Electrochemiluminescence (ECL) serves as a powerful means of trace analysis due to its combination of accurate electrochemical control and high exceptional sensitivity.[6,8] The properties of luminescent molecules directly determine the detection limit of the ECL system.[9] Metal−organic frameworks (MOFs) consist of metal nodes and organic ligands, and their tailorable structures and dense active sites endow them as ideal ECL emitters.[10] In particular, Hf-MOF has enhanced Hf−O bond strength, which confers superior stability in aqueous solution systems and thus provides a material basis for the analysis of complex water matrices.[11] However, relying solely on its intrinsic structural properties, the ECL emission efficiency and electron transfer rate of Hf-MOF still cannot meet the high-sensitivity detection requirements for trace analysis.[12] Consequently, the rational design of the Hf-MOF framework structure serves as a central link in building high-performance ECL sensing platforms.[13] The synergistic effect of dual-ligand MOFs provides a promising strategy for improving the ECL performance of MOF-based systems compared to single-ligand MOFs.[14] For example, Zhu et al. reported a mixed-ligand metal−organic framework (MOF) that was constructed through the coordinative coassembly of 9,10-di(p-carboxyphenyl)anthracene (DPA) and 1,4-diazabicyclo[2.2.2]octane (D-H_2) and that exhibited self-enhanced ECL.[15] Bu et al. employed tris(4,4′-dicarboxylic acid 2,2′-bipyridyl) ruthenium(II) dichloride ($Ru(dcbpy)_3^{2+}$) and ethylenediamine (EDA) to construct a dual-ligand

Received: November 10, 2025
Revised: February 3, 2026
Accepted: February 10, 2026
Published: February 17, 2026

https://doi.org/10.1021/acs.analchem.5c07097
Anal. Chem. 2026, 98, 6139−6148

coordination polymer (Zn−Ru−EDA) with self-enhanced ECL properties, which enabled highly sensitive detection of procalcitonin (PCT).[16] Inspired by the above work, a dual-ligand design strategy was implemented in the present study to simultaneously enhance the ECL emission efficiency and charge transfer efficiency of Hf-MOF.[17] Among the ligands, biphenyl-4,4′-dicarboxylic acid (BPDC) was selected as the rigid framework ligand of Hf-MOFs, owing to its unique molecular structure, high coordination compatibility with Hf^{4+}, and excellent functional synergism with porphyrin ligands. First, the dicarboxyl groups of BPDC molecules can form stable multidentate coordination structures with Hf^{4+}. Compared with conventional monocarboxyl ligands, this multidentate coordination mode significantly enhances the structural stability of the Hf-MOF framework, enabling it to effectively resist structural collapse induced by solvation effects in aqueous detection systems and thereby meeting the practical requirements for complex water sample analysis. Second, the biphenyl core of the BPDC molecule possesses a favorable $\pi-\pi$-electron-conjugated system, which can act as an efficient electron transfer bridge to accelerate charge transport within the framework. Overall, selecting BPDC as the rigid framework ligand ensures the structural stability and porosity of the Hf-MOFs, while introducing the synergistic porphyrin functional ligand enables the construction of an efficient electron transfer network, effectively improving electron transfer and ECL efficiencies. This dual-ligand synergy endowed Hf-MOF with efficient luminescence ability, overcoming the challenge that stability and luminescence efficiency were difficult to balance in single-ligand MOFs for ECL applications.[18]

Although synergistic enhancements in the luminescence performance and stability of Hf-MOF had been achieved via dual-ligand design, the overall signal intensity of ECL systems depended not only on the performance of the emitter (Hf-MOF) but also strongly on the activation efficiency of the coreactant system.[19] Notably, the insufficient efficiency of conventional coreactant accelerators in capturing coreactants became a critical bottleneck that restricted the improvement of catalytic efficiency in our ECL sensing system.[20] To address this issue, the present study innovatively introduced La-deficient $LaCoO_3$ (LCO-V_{La}) as a coreactant accelerator, whose core advantage lay in the establishment of an "adsorption-catalytic"-integrated interface (Scheme 1A).[2,21] On the one hand, La vacancy (V_{La}) regulated the surface electronic structure and charge distribution of $LaCoO_3$ (LCO), thereby significantly enhancing the adsorption capacity for potassium persulfate ($K_2S_2O_8$).[22] V_{La} weakened the O−O bond in $S_2O_8^{2-}$ via directional stretching, reduced its bond cleavage energy barrier, and thus enabled the efficient catalytic activation of $K_2S_2O_8$.[23] On the other hand, the Co^{3+}/Co^{4+} redox couple on the surface of LCO-V_{La} could act as an efficient electron-transfer catalyst, which catalyzed the activation of adsorbed $S_2O_8^{2-}$ to generate highly reactive sulfate radicals ($SO_4^{\bullet-}$). These radicals could undergo efficient electron-transfer reactions with Hf-MOF luminophores, thereby significantly enhancing the ECL efficiency of the system. The synergistic mechanism effectively overcame the efficiency limitation of traditional coreactant accelerators caused by their single catalytic function and laid an important foundation for the efficient amplification of ECL signals.[24] In conclusion, the excellent optical stability of the dual-ligand Hf-MOF was synergistically integrated with the catalytic activity of LCO-V_{La}, which significantly improved the sensitivity and reproducibility of the ECL sensing system through a DNA-mediated cyclic amplification strategy. The proposed strategy provides a novel approach for the accurate analysis of trace algal toxins in complex aqueous environments.

Scheme 1. (A) Adsorption of $S_2O_8^{2-}$ on LCO-V_{La}; (B) the construction process of the sensor

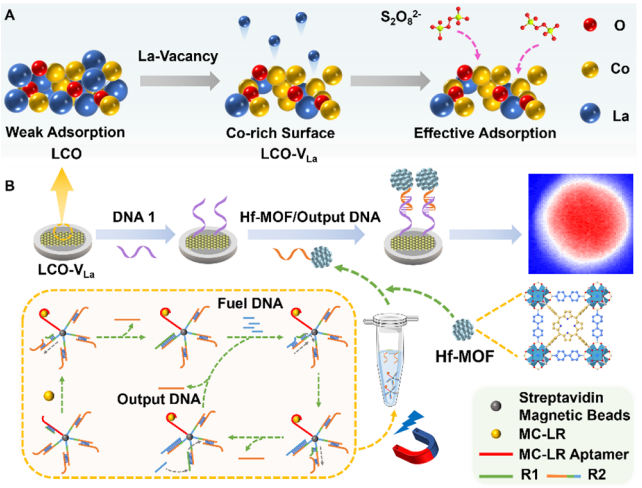

EXPERIMENTAL SECTION

Materials

Hafnium(IV) chloride ($HfCl_4$, 99.5%), biphenyl-4,4′-dicarboxylic acid (BPDC, 97%), *N*,*N*-dimethylformamide (DMF), and methanol (MeOH, 99%) were purchased from Macklin. Streptavidin magnetic beads with a particle size of 0.5 μm (Shanghai Shenggong Bioengineering Technology Service Co., Ltd.) were used without further treatment. Meso-tetra(4-carboxyphenyl)porphyrin (TCPP, 97%), $La(NO_3)_3{\cdot}6H_2O$, $Co(NO_3)_2{\cdot}6H_2O$, $NH_3{\cdot}H_2O$, ethylene glycol, and CH_3COOH were purchased from Aladdin. The ECL measurements were performed in phosphate buffer solution (PBS, 0.10 M KH_2PO_4/Na_2HPO_4, pH 7.4). The 5 mM $[Fe(CN)_6]^{3-/4-}$ solution containing 0.10 M KCl electrolyte was employed for electrochemical impedance spectroscopy (EIS). The ultrapure water with a specific resistivity (≥18.2 MΩ·cm) was obtained from a Millipore water purification system.

Synthesis of Hf-MOF

Initially, 8 mL of DMF was mixed with 96 mg of $HfCl_4$ and 72.3 mg of BPDC. 60 mg portion of TCPP powder was added separately to the mixed solution to obtain a sample named HBT after stirring for 30 min. The resulting mixture was then transferred to an autoclave and maintained at 150 °C for 24 h. DMF and MeOH were used to wash the centrifuged product, which was then dried at 60 °C.

Synthesis of LCO-V_{La}

LCO-V_{La} nanoparticles were prepared by the sol−gel method. Specifically, 10 mmol of $La(NO_3)_3{\cdot}6H_2O$, 10 mmol of $Co(NO_3)_2{\cdot}6H_2O$, and 40 mmol of citric acid were dissolved in 300 mL of ultrapure water. The mixture was stirred at 80 °C to obtain a clear solution, and ammonia was added to adjust the pH to about 9. Subsequently, 40 mmol of ethylene glycol was added and heated to form a viscous purple hydrogel. The hydrogel was heated at 250 °C for 5 h to obtain a xerogel, which was ground into a fine powder and calcined at 700 °C for 5 h in a muffle furnace to obtain LCO. After dispersing 250

https://doi.org/10.1021/acs.analchem.5c07097
Anal. Chem. 2026, 98, 6139−6148

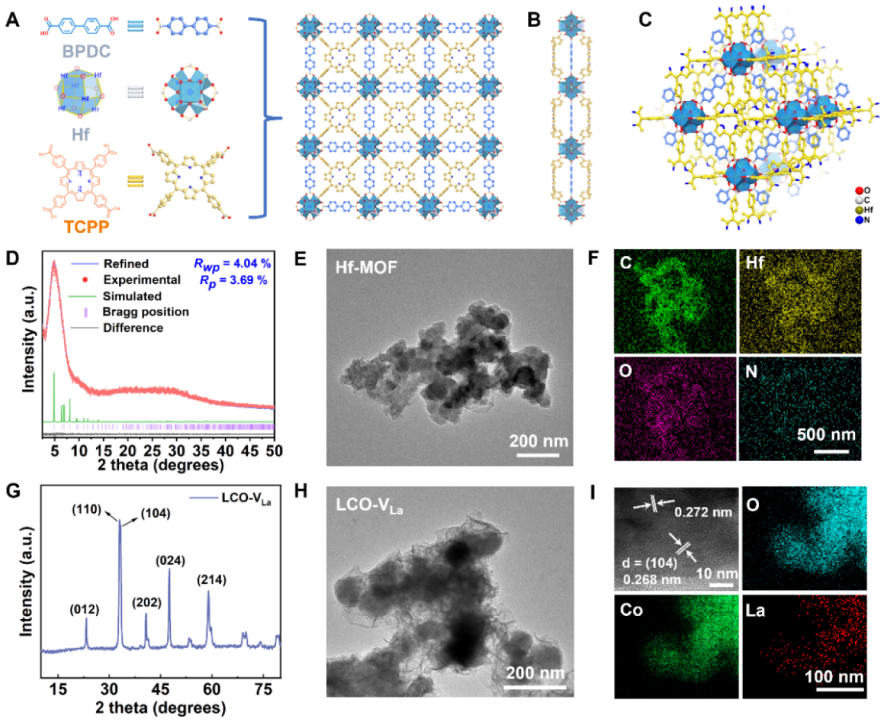

Figure 1. (A) The synthesis process of Hf-MOF. (B) Side view of the Hf-MOF. (C) Perspective view of the Hf-MOF. (D) PXRD patterns of Hf-MOF: experimental data (red dots) and simulated results (blue line). (E) TEM image of the Hf-MOF. (F) Elemental mapping images of C, Hf, O, and N in Hf-MOF. (G) XRD patterns of LCO-V_{La}. (H) TEM images of LCO-V_{La}. (I) HRTEM image and elemental mapping images of O, La, and Co in LCO-V_{La}.

mg of LCO in 20 mL of ultrapure water, 12 mL of glacial acetic acid was added and stirred for 20 min. The mixture was centrifuged, washed several times with water and ethanol, and dried under vacuum at 60 °C.

Fabrication of the ECL Biosensor

As shown in Scheme 1B, 6 μL of a 2 mg/mL LCO-V_{La} solution was directly coated onto the polished electrode. After the electrode was air-dried naturally, it was immersed in a 10 μM DNA1 solution for incubation. Following this, Hf-MOF/output DNA was further modified onto the electrode surface and incubated for 20 min. The prepared working electrode was measured in 10 mL PBS solution (pH 7.4) using a standard three-electrode system.

Construction of MC-LR Sensor by Fuel DNA Replacement Cycle Amplification

The 100 μL streptavidin magnetic beads were activated with 1-ethyl-3-(3-(dimethylamino)propyl)carbodiimide (EDC) (0.1 M) and *N*-hydroxysuccinimide (NHS) (0.025 M) for 1 h. The activated beads were then incubated with equal amounts of two types of double strands, namely, the MC-LR aptamer (10 μM)/R1 (10 μM) double strand and the output DNA (10 μM)/R2 (10 μM) double strand, for 6 h to achieve binding. After magnetic separation, the resulting complexes were dispersed in 100 μL of Tris-EDTA (TE) buffer solution. 40 μL of the aforementioned dispersion was taken and mixed with 5 μL of MC-LR solutions at various concentrations, and the reaction was allowed to proceed for 2 h. Subsequently, 10 μL of fuel DNA (10 μM) was added, and the reaction was continued for another 2 h. Subsequently, the supernatant collected via magnetic separation was mixed with 6 μL of Hf-MOF (2 mg/mL) suspensions at different concentrations to form Hf-MOF/output DNA.

RESULTS AND DISCUSSION

Characterization of Materials

Powder X-ray diffraction (PXRD) analysis and theoretical structural simulations using Materials Studio (MS) were conducted to determine the crystalline structure of Hf-MOF. Based on previous studies,[25] combined with theoretical structure simulation and Pawley refinement, the unit cell parameters for Hf-MOF were established as $a = b = 17.9164$ Å, $c = 13.6022$ Å, with angles $\alpha = \beta = \gamma = 90°$, fitting within the P4/mmm space group. The residual factors (R_p = 3.69% and R_{wp} = 4.04%) confirmed the credibility of the calculation model (Figure 1A–C). The PXRD peaks of Hf-MOF observed at 4.94° and 9.5° corresponded to the (100) and (111) crystallographic planes, respectively (Figure 1D).

The surface morphology and microstructure of the Hf-MOF were characterized via transmission electron microscopy (TEM). As presented in Figure 1E, Hf-MOF was observed to exhibit irregular nanosheet-like aggregates. Additionally, elemental mapping results demonstrated the uniform distribution of C, O, Hf, and N elements throughout the Hf-MOF (Figure 1F). For LCO-based samples, the XRD patterns of LCO-V_{La} matched those of previously reported LCO (JCPDS no. 48-0123), indicating a similar crystal structure. Characteristic diffraction peaks were observed at 2θ = 23.2°, 32.8°, 33.3°, 40.6°, 47.5°, and 58.9°, corresponding to the (012), (110), (104), (202), (024), and (214) crystal planes, respectively (Figure 1G). The structural and morphological characteristics of LCO-V_{La} and LCO were further characterized by TEM and selected area electron diffraction (SAED). The results demonstrated that both LCO (Figure S1A–B) and LCO-VLa (Figure 1H) exist as uniformly dispersed spherical nanoparticles with an average size of approximately 100 nm.

https://doi.org/10.1021/acs.analchem.5c07097
Anal. Chem. 2026, 98, 6139−6148

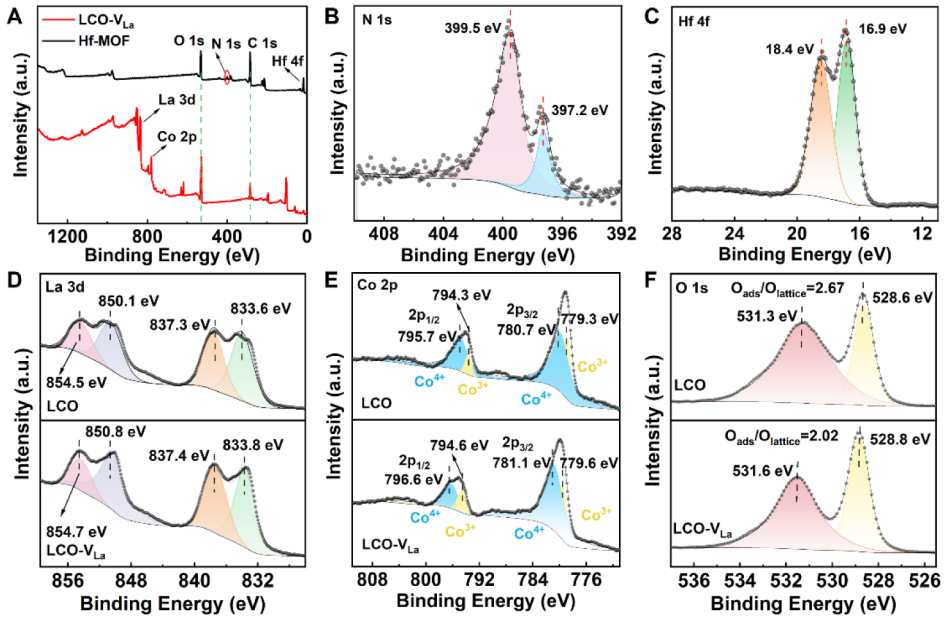

Figure 2. (A) XPS survey spectrum of LCO-V_{La} and Hf-MOF. (B−C) XPS high-resolution spectra of N 1s and Hf 4f in the Hf-MOF. (D−F) XPS high-resolution spectra of La 3d, Co 2p, and O 1s in LCO-V_{La}.

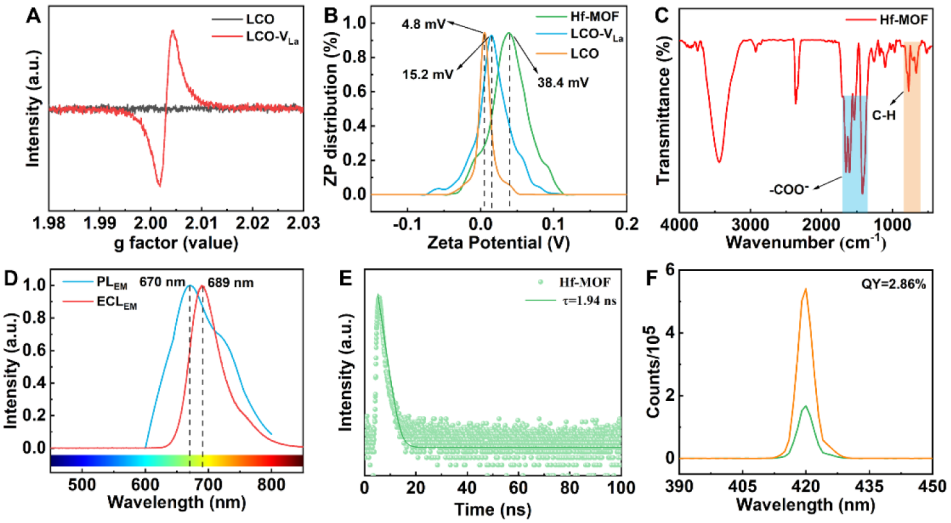

Figure 3. (A) EPR spectra of LCO and LCO-V_{La}. (B) Zeta potential curves of Hf-MOF, LCO, and LCO-V_{La}. (C) FTIR spectra of the Hf-MOF. (D) PL emission spectra (blue line) and ECL spectrum (red line) of the Hf-MOF. Fluorescence lifetime (E) and QY curves (F) of the Hf-MOF.

Elemental mapping results revealed that La, Co, and O elements were homogeneously distributed in both materials, confirming the successful preparation of LCO and LCO-V_{La} (Figure 1I and Figure S1C−E). Owing to the introduction of La vacancies (V_{La}), the (104) lattice fringe spacing in LCO was 0.268 nm, whereas in LCO-V_{La}, the (104) lattice fringe spacing increased to 0.272 nm (Figure S1F). To verify crystal structure integrity, selected area electron diffraction (SAED, Figure S2) further confirmed that LCO-V_{La} retained characteristic lattice planes, demonstrating that V_{La} did not disrupt its basic crystal structure.

The chemical states of elements in the prepared samples were analyzed via X-ray photoelectron spectroscopy (XPS) characterization. In the XPS full spectrum of the Hf-MOF sample, characteristic peaks corresponding to C, N, and Hf elements were observed (Figure 2A). The high-resolution C 1s spectrum exhibited two characteristic peaks with binding energy centers located at 284.8 and 288.2 eV, which were assigned to C−O and C═O bonds, respectively (Figure S3A). The O 1s spectrum showed a peak at 531.5 eV (Figure S3B). In Figure 2B, the two characteristic peaks in the N 1s spectrum at 397.2 and 399.5 eV corresponded to C═N and C−N bonds, respectively. The Hf 4f spectrum could be fitted into two peaks with binding energies of 18.4 and 16.9 eV, corresponding to the Hf $4f_{5/2}$ and Hf $4f_{7/2}$ orbitals, respectively, indicating the presence of Hf-oxygen bonds in Hf-MOF (Figure 2C). As shown in Figure 2D, lanthanum existed in the La^{3+} oxidation state in both pristine LCO and LCO-V_{La}. The binding energies of La $3d_{5/2}$ and La $3d_{3/2}$ orbitals were 833.8 and 850.8 eV in LCO-V_{La}, respectively. The La 3d orbital peaks were accompanied by distinct satellite peaks, which originated from electron transitions involving the 4f orbital.[26] The binding energy of the La 3d orbital in LCO-V_{La} exhibited a positive shift relative to that in pristine LCO,

https://doi.org/10.1021/acs.analchem.5c07097
Anal. Chem. 2026, 98, 6139−6148

and this was due to the formation of V_{La}, which reduced the effective positive charge of the system.[27] In Figure 2E, the Co 2p orbitals split into two characteristic peaks ($2p_{3/2}$ and $2p_{1/2}$) due to the spin−orbit coupling effect. Specifically, the binding energies of $2p_{3/2}$ and $2p_{1/2}$ corresponding to Co^{3+} were 779−780 eV and 794−795 eV, respectively. Co^{4+} exhibited a higher oxidation state than Co^{3+}, with the binding energies of its $2p_{3/2}$ and $2p_{1/2}$ being 780.5−782 eV and 795.5−797 eV, respectively. Quantitative analysis of the integrated area of the $2p_{3/2}$ characteristic peak showed that the area ratio of Co^{4+}/Co^{3+} in the LCO sample was 2.04, while that in the LCO-V_{La} sample was increased to 2.67, indicating a higher proportion of Co^{4+} in the LCO-V_{La}.[28] The essence of this phenomenon was that the formation of V_{La} introduced additional negative charges, and the valence state transition from Co^{3+} to Co^{4+} could achieve charge compensation for the system, thereby maintaining the electrical neutrality of the crystal structure.[29]

The O 1s of LCO-V_{La} exhibited two characteristic peaks at 531.6 and 528.8 eV, corresponding to oxygen adsorption vacancies (V_o) on the sample surface and lattice oxygen in the sample, respectively (Figure 2F). The ratio of the oxygen adsorption peak area to the lattice oxygen peak area ($O_{ads}/O_{lattice}$) was used to evaluate the concentration of V_o.[30] Compared with LCO, the concentration of V_o in LCO-V_{La} decreased from 2.62 to 2.02, indicating that the lattice distortion induced by V_{La} modified the coordination environment of oxygen atoms (e.g., enhancing the Co−O bond energy) and thus suppressed the formation of V_o. The binding energy of the C 1s orbital in LCO-V_{La} was shifted toward the higher binding energy region compared with that in LCO (Figure S3C). This shift occurred because V_{La} introduction reduced the electron cloud density around the C atoms, which increased the binding energy of the C 1s electrons and consequently shifted the peak to a higher binding energy. These results further confirmed that V_{La} was the main characteristic defect in this system.

Electron paramagnetic resonance (EPR) spectroscopic analysis (Figure 3A) confirmed the existence of unpaired electronic states caused by V_{La} in the material. The EPR signal intensity of LCO-V_{La} was significantly enhanced when compared to the unmodified LCO, which indicated a notable increase in the concentration of V_{La}. This characteristic signal variation demonstrated that V_{La} defects had been successfully incorporated into the material structure. The zeta potential distribution curves of the three materials (Hf-MOF, LCO, and LCO-V_{La}) were presented in Figure 3B. The zeta potential peak of Hf-MOF was observed at approximately 38.4 mV, that of LCO at around 4.8 mV, whereas the peak of LCO-V_{La} exhibited a shift to 15.2 mV. The introduction of V_{La} led to the redistribution of charges among surrounding ions, and some Co^{3+} was oxidized to Co^{4+} to maintain the overall electrical neutrality of the material, which was consistent with the results obtained via XPS.[31]

Optical Features of Hf-MOF

The chemical structure of Hf-MOF was characterized by Fourier transform infrared spectroscopy (FTIR). The out-of-plane bending vibration of the C−H bond on the benzene ring exhibited a characteristic peak in the range 720−670 cm^{-1} (Figure 3C). Two absorption bands appearing in the ranges of 1600−1546 cm^{-1} and 1420−1440 cm^{-1} corresponded to the asymmetric stretching vibration (ν_{asym}) and symmetric stretching vibration (ν_{sym}) of the $-CO_2^-$ carboxylate group, respectively.[32] The presence of these characteristic peaks indicated that coordination interactions were formed between TCPP and the Hf metal in Hf-MOF.

To fully elucidate the optical properties of the Hf-MOF, ultraviolet−visible (UV−vis) spectroscopy was employed for characterization. As depicted in Figure S3D, the UV−vis spectrum of Hf-MOF exhibited a prominent absorption peak at 437 nm, indicating the presence of a porphyrin ring-conjugated structure in the molecule. Additionally, two distinct secondary peaks emerged at 528 and 564 nm, a phenomenon arising from the enhanced symmetry of the porphyrin ring upon coordination with Hf metal ions that led to the simplification of the Q-band into two primary peaks, thereby confirming the successful formation of a coordination interaction between Hf metal and the porphyrin macrocycle.[33] Further investigation into the optical properties was conducted via analyses of the photoluminescence (PL) excitation spectra and ECL emission spectra. At an excitation wavelength of 420 nm, the PL emission spectrum of the Hf-MOF displayed a characteristic peak at 670 nm, whereas its ECL spectrum exhibited a distinct emission maximum at 689 nm (Figure 3D). The peak of ECL emission was red-shifted compared to the PL emission, indicating that the ECL emission originated from the surface state rather than the band gap emission. The photophysical properties of the Hf-MOF were systematically characterized by time-resolved fluorescence spectroscopy (TRFS) and transient fluorescence spectroscopy. The fluorescence lifetime (τ) and quantum yield (QY) of Hf-MOF were 1.94 ns and 2.86%, respectively (Figure 3E−F), indicating that the Hf-MOF possessed the potential to serve as an excellent luminophore.

Possible Luminescence Mechanism

To verify the possible luminescent mechanism of the Hf-MOF, electrochemical tests and ECL measurements were employed for characterization in this study. Figure S4A showed that when Hf-MOF was introduced into the phosphate-buffered solution (PBS, pH 7.4) with a quantified amount of $K_2S_2O_8$, CV measurements detected the presence of an oxidation peak within the potential range of −1.2 to −0.23 V (vs Ag/AgCl). DPV curves showed two clear oxidation peaks at −1.07 V and −0.61 V in Figure S4B, providing direct evidence for the proposed two-step electron transfer mechanism. In addition, in 0.1 M PBS (0.1 M KH_2PO_4/Na_2HPO_4, pH 7.4) containing 80 mM $K_2S_2O_8$, 5,5-dimethyl-1-pyrroline-*N*-oxide (DMPO) was used as the $SO_4^{\bullet-}$ radical trapping agent, and electron paramagnetic resonance (EPR) measurements were performed on LCO and LCO-V_{La}, respectively (Figure S4C). The results demonstrated that the presence of La vacancies facilitated the generation of a greater quantity of sulfate radicals ($SO_4^{\bullet-}$) from the dissociation of $S_2O_8^{2-}$, thereby effectively enhancing the catalytic activation capability of LCO-V_{La} toward $K_2S_2O_8$. ECL tests were performed on a glassy carbon electrode (GCE), LCO/Hf-MOF, and LCO-V_{La}/Hf-MOF in PBS containing 80 mM $K_2S_2O_8$ within the potential range of 0 to −1.2 V (Figure S4D). The results showed that the presence of vacancies significantly enhanced the ECL intensity of Hf-MOF, confirming that defects could effectively promote the ECL performance of Hf-MOF.

Using LCO and LCO-V_{La} as model systems, the adsorption and catalytic mechanisms of V_{La} toward $S_2O_8^{2-}$ were investigated in depth via first-principles calculations. In Figure

https://doi.org/10.1021/acs.analchem.5c07097
Anal. Chem. 2026, 98, 6139−6148

4A, the adsorption energy of $S_2O_8^{2-}$ on the LCO-V_{La} (104) surface (E_{ads} = −2.76 eV) was significantly lower than that on the LCO (104) surface (E_{ads} = −1.58 eV), indicating that the incorporation of V_{La} remarkably enhanced the adsorption capacity of LCO-V_{La} for $S_2O_8^{2-}$ compared to that of LCO. Notably, the O−O bond length of $S_2O_8^{2-}$ adsorbed on the LCO-V_{La} surface was elongated to 1.54 Å, which exceeded that of $S_2O_8^{2-}$ adsorbed on the LCO surface (1.48 Å). The above results confirmed that V_{La} could accelerate the weakening and cleavage process of the O−O bond in $S_2O_8^{2-}$ through more effective elongation of this bond, ultimately significantly enhancing the catalytic activity of the material.[34]

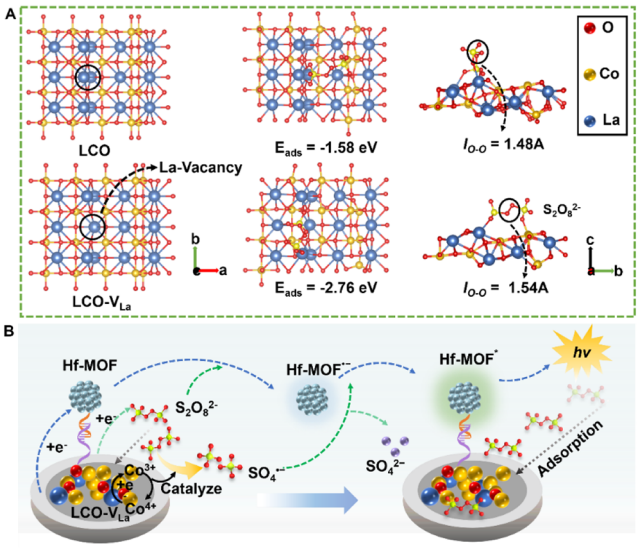

Figure 4. (A) Top view of LCO-V_{La} (104) and LCO (104) surfaces and the adsorption energy and bond length of $S_2O_8^{2-}$ on these surfaces. (B) Schematic illustration of the ECL emission mechanism of Hf-MOF.

Moreover, the adsorption and catalytic processes of LCO and LCO-V_{La} toward $S_2O_8^{2-}$ were elucidated via in situ electrochemical Fourier transform infrared (FTIR) measurements, which were carried out under N_2-saturated conditions in a 0.1 M PBS (pH 7.4) containing 80 mM $K_2S_2O_8$, with the applied potential scanned negatively from 0 V to −1.2 V at 100 mV intervals (Figure S5). As the applied potential was scanned negatively, characteristic peaks corresponding to the O−O stretching vibration of $S_2O_8^{2-}$ and the S═O stretching vibration of its reduction product SO_4^{2-} were observed on the surfaces of both LCO and LCO-V_{La} electrodes. On the LCO electrode surface (Figure S5A), the catalytic reduction reaction of $S_2O_8^{2-}$ was significantly enhanced when the applied potential was more negative than −0.4 V. The intensities of the O−O peak (891 cm^{-1}) and the S═O peak (975 cm^{-1}) gradually decreased as the applied potential became more negative. This was attributed to the weak initial adsorption of

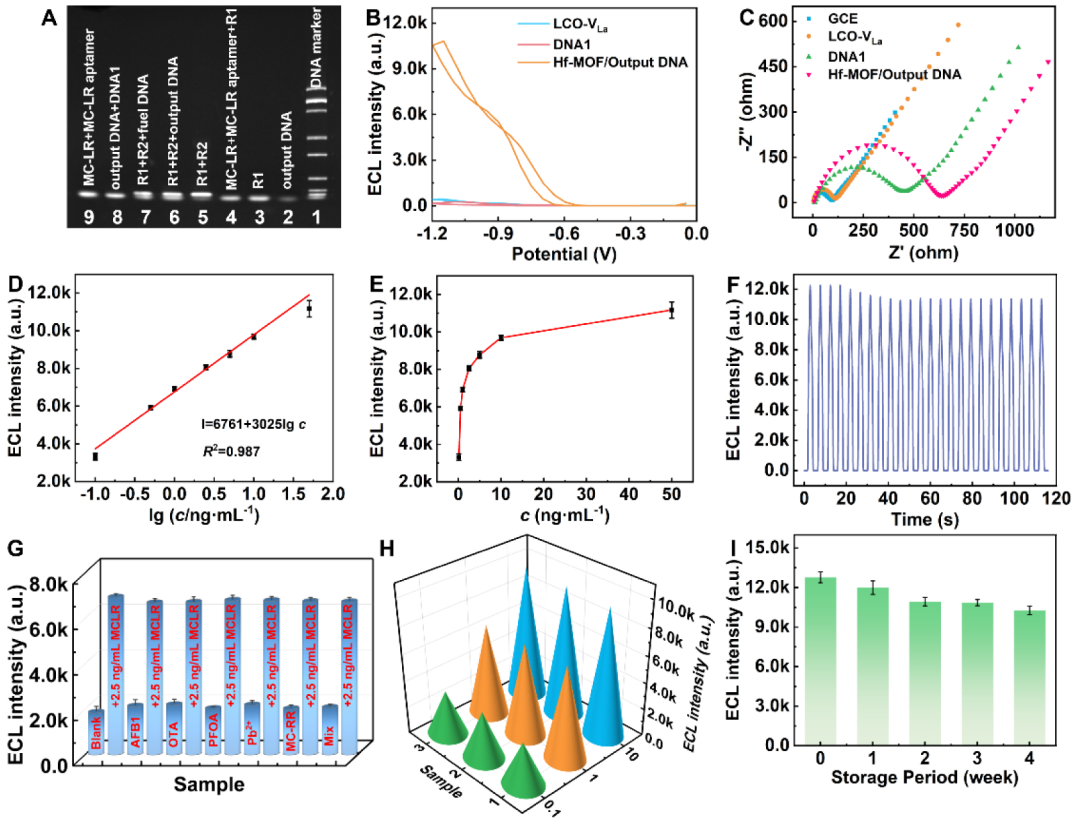

Figure 5. (A) PAGE images of lanes 1−9 (from right to left): DNA marker, output DNA, R1, MC-LR + MC-LR aptamer + R1, R1 + R2, R1 + R2 + output DNA, R1 + R2 + fuel DNA, output DNA + DNA1, MC-LR + MC-LR aptamer. (B) ECL intensity-potential curve of the biosensor construction process. (C) EIS characterization of sensor construction. (D) The calibration curve (0.1−50 ng/mL). (E) Logarithmic curve. (F) Stability of the ECL sensor in the presence of MC-LR (50 ng/mL). (G) ECL intensity of the sample: 25 ng/mL interfering substances (AFB1, OTA, PTOA, Pb^{2+}, and MC-RR), 2.5 ng/mL MC-LR, and their mixtures. (H) Reproducibility of the proposed ECL biosensor at concentrations of 0.1, 10, and 50 ng/mL. (I) Storage stability of an ECL biosensor at a concentration of 50 ng/mL.

https://doi.org/10.1021/acs.analchem.5c07097
Anal. Chem. 2026, 98, 6139−6148

adsorbed $S_2O_8^{2-}$ on the LCO electrode surface, which was gradually consumed and ultimately depleted over the course of electrocatalysis, revealing the inadequate adsorption and activation capabilities of LCO toward $S_2O_8^{2-}$.[35] On the LCO-V_{La} electrode, the reduction of $S_2O_8^{2-}$ was initiated at the initial phase of negative potential scanning (Figure S5B). As the applied potential became more negative, the O−O peak exhibited a red shift (from 903 to 896 cm^{-1}) while its peak intensity increased continuously. This indicated that the O−O bond underwent elongation and continuous cleavage, which was in good agreement with the DFT calculation results. With the cleavage of the O−O bond, the S═O peak exhibited a blue shift (from 970 to 983 cm^{-1}) while retaining its high peak intensity, indicating the continuous generation of SO_4^{2-}.[36] These results demonstrated that the presence of La vacancies effectively enhanced the electrocatalytic activity of LCO-V_{La} toward $S_2O_8^{2-}$.

Figure 4B further illustrates the luminescence mechanism of the system. Initially, $K_2S_2O_8$ underwent direct cathodic reduction at the electrode surface, producing a small quantity of sulfate radical anions ($SO_4^{\bullet-}$) (eq 1). When LCO-V_{La} was employed as a coreactant to adsorb $S_2O_8^{2-}$, the Co^{4+} on the surface of LCO-V_{La} first obtained electrons from the electrode surface and was reduced to Co^{3+}, thereby promoting the reduction of $S_2O_8^{2-}$ to generate more $SO_4^{\bullet-}$ (eqs 2 and 3). As a luminophore, Hf-MOF initially underwent reduction on the electrode surface by accepting electrons to generate its radical anion (Hf-MOF$^{\bullet-}$), which then reacted with $SO_4^{\bullet-}$ in the system to form the excited state Hf-MOF* and ultimately emitted a strong ECL signal through a radiative transition (eqs 4−6):

$$S_2O_8^{2-} + e^- \rightarrow SO_4^{\bullet-} + SO_4^{2-} \quad (1)$$

$$Co^{4+} + e^- \rightarrow Co^{3+} \quad (2)$$

$$Co^{3+} + S_2O_8^{2-} \rightarrow Co^{4+} + SO_4^{\bullet-} + SO_4^{2-} \quad (3)$$

$$\text{Hf-MOF} + e^- \rightarrow \text{Hf-MOF}^{\bullet-} \quad (4)$$

$$SO_4^{\bullet-} + \text{Hf-MOF}^{\bullet-} \rightarrow SO_4^{2-} + \text{Hf-MOF}^* \quad (5)$$

$$\text{Hf-MOF}^* \rightarrow \text{Hf-MOF} + h\nu \quad (6)$$

Feasibility Investigation of Sensing Approach

The mobility of DNA samples was analyzed via polyacrylamide gel electrophoresis (PAGE) to validate the feasibility of the approach (Figure 5A), and the corresponding DNA sequences were provided in Table S1. The rightmost lane corresponded to the DNA marker, with lanes 2−3 corresponding to output DNA and R1, respectively. Lane 4 displayed the hybridization product of MC-LR, MC-LR aptamer, and R1. Comparison with lane 9 revealed that the presence of R1 did not disrupt the stable binding between MC-LR and its aptamer. When R1 and R2 were coadded in lane 5, the appearance of bands with a higher molecular weight indicated the formation of the R1/R2 hybrid products. When output DNA was added (lane 6), the number of bands was consistent with that in lane 5, indicating that the introduction of output DNA did not disrupt the hybrid products formed by R1 and R2. Lane 7 contained the mixed system of R1 + R2 + fuel DNA, and its migration rate differed significantly from that in lane 5, confirming that R2 preferentially hybridized with fuel DNA. Lane 8 showed the binding complex of DNA1 and output DNA, and the upward migration shift of the band indicated the formation of their hybrid duplex. These PAGE results confirmed the feasibility of the biosensor strategy.

ECL-potential profiles and electrochemical impedance spectroscopy (EIS) were utilized to characterize the fabrication process of the biosensor. After the sequential modification of the bare glassy carbon electrode with LCO-V_{La} (green line) and DNA1 (blue line), the ECL signal gradually decreased, whereas the ECL intensity increased significantly upon subsequent addition of the luminophore Hf-MOF/output DNA (Figure 5B). The Randles equivalent circuit (Figure 5C) contained simulated parameters for the electron transfer resistance (R_{et}), with specific values provided in Table S2. The impedance value gradually increased with the stepwise modification of the electrode, which proved the successful preparation of the sensor.

Performance Evaluation

The analytical performance of the constructed ECL biosensor was systematically evaluated under the optimized experimental conditions (Figure S6). The ECL signal intensity exhibited a significant upward trend with the gradient increase of MC-LR concentration from 0.1 to 50 ng/mL. Figure 5D indicated that the ECL response intensity presented a good linear relationship with the logarithm of MC-LR concentration, and the linear relationship was $I = 6761 + 3025 \lg c$ ($R^2 = 0.987$). The limit of detection (LOD) was calculated to be 0.033 ng/mL (S/N = 3, the detailed calculation process is shown in the Supporting Information). Notably, within the wide concentration range of 0.1 to 50 ng/mL, the ECL intensity was positively correlated with MC-LR concentration, and the curve conformed to the logarithmic function characteristics (Figure 5E). Compared with the reported detection strategies in the literature, the sensor prepared in this study exhibited an excellent detection performance (Table S3).

In addition, selectivity, reproducibility, and stability were also investigated as key parameters for evaluating the performance of the biosensor. The biosensor could still maintain 92.6% of its initial relative signal after 24 cycles, illustrating the good stability of the biosensor in Figure 5F. Typical interfering substances, including aflatoxin B1 (AFB1), ochratoxin A (OTA), perfluorooctanoic acid (PFOA), lead ions (Pb^{2+}) and microcystin-RR (MC-RR), were selected to investigate their effects on the detection of the target analyte. As shown in Figure 5G, even when the concentration of the interfering substances was 10 times higher than that of the target MC-LR, no significant interference was observed in the detection of the target, indicating that the sensor exhibited excellent anti-interference ability. Furthermore, the interfering anions (Cl^-, HCO_3^-) at varying concentrations were introduced to investigate whether these anions in real water samples would affect the adsorptive catalytic activity of $S_2O_8^{2-}$ on the LCO-V_{La} surface and thus impact the sensor performance. As shown in Figure S7, even in the presence of high-concentration interfering ions, the relative standard deviation (RSD) of the ECL signal of the substrate material remained below 1.7%, while the RSD values of the sensor performance were all less than 3.5%. These results indicated that the interfering anions exerted negligible effects on the adsorptive catalytic performance of LCO-V_{La}, and the constructed sensor possessed an excellent anti-interference capability. The reproducibility of the sensor was evaluated by detecting different concentrations of the MC-LR antigen. As

https://doi.org/10.1021/acs.analchem.5c07097
Anal. Chem. 2026, 98, 6139−6148

shown in Figure 5H, stable ECL response signals were consistently obtained across different MC-LR concentrations (0.1, 10, and 50 ng/mL, n = 3), confirming the good reproducibility of the fabricated sensor. The results of the long-term stability test showed that the ECL intensity of the sensor could still maintain 80.2% of its initial value after 4 weeks of storage at 4 °C (Figure 5I), indicating that the detection performance had exhibited long-term stability. In conclusion, the ECL sensing platform constructed in this study exhibits promising application potential in the field of trace detection for bioanalysis.

Sample Analysis

Recovery tests were performed by adding MC-LR at concentrations of 5.0, 10.0, and 30.0 ng/mL to freshwater samples, real wastewater, seawater, and water samples with a high organic content, aiming to evaluate the performance of the proposed biosensor. The recoveries from five parallel measurements ranged from 99.2% to 101%, with RSDs of 0.36% to 2.86% (Table S4). These results fully confirmed that the fabricated sensor exhibited excellent anti-interference capability and stable detection performance, even in complex water matrices.

CONCLUSION

An integrated sensing platform that coupled the LCO-V_{La} adsorption-catalytic interface with the Hf-MOF luminescent substrate was developed, enabling the accurate determination of MC-LR at the ultratrace level. First, the presence of V_{La} promoted the efficient adsorption of $S_2O_8^{2-}$ at the interface, constructing an integrated "adsorption-catalytic" interface. The O−O bond was stretched (from 1.48 to 1.54 Å), which promoted the cleavage of the bond and achieved efficient catalytic activation of $K_2S_2O_8$. Second, the Hf-MOF was constructed via the dual-ligand strategy combining rigid and functional ligands. The rigid ligands suppressed framework hydrolysis, while the porphyrin ligands expanded π-conjugation and reduced exciton binding energy. These combined effects concurrently boosted luminescence efficiency and long-term chemical stability, thereby furnishing a robust ECL platform for subsequent signal amplification. Overall, this strategy offered a novel approach for the precise monitoring of trace algal toxins in complex aquatic systems.

ASSOCIATED CONTENT

Supporting Information

The Supporting Information is available free of charge at https://pubs.acs.org/doi/10.1021/acs.analchem.5c07097.

Apparatus, SEM and TEM images, selected area electron diffraction (SAED) image, XPS high-resolution spectra, UV−vis diffuse reflectance spectrum, CV curves, DPV curves, optimizing conditions, in-situ electrochemical Fourier transform infrared spectroscopic test, DNA pretreatment, adsorption energy calculation, and the calculation of LOD (PDF)

AUTHOR INFORMATION

Corresponding Authors

Rui Feng − *Collaborative Innovation Center for Green Chemical Manufacturing and Accurate Detection, Key Laboratory of Chemical Sensing & Analysis in Universities of Shandong, School of Chemistry and Chemical Engineering, University of Jinan, Jinan 250022, P. R. China*; Email: ruifeng8804@gmail.com

Yu Du − *School of Water Conservancy and Environment, University of Jinan, Jinan, Shandong 250022, China*; orcid.org/0000-0002-9002-8845; Email: duyu_ujn@163.com

Qin Wei − *Collaborative Innovation Center for Green Chemical Manufacturing and Accurate Detection, Key Laboratory of Chemical Sensing & Analysis in Universities of Shandong, School of Chemistry and Chemical Engineering, University of Jinan, Jinan 250022, P. R. China; Department of Chemistry, Sungkyunkwan University, Suwon 16419, Republic of Korea*; orcid.org/0000-0002-3034-8046; Email: sdjndxwq@163.com

Authors

Yamei Li − *Collaborative Innovation Center for Green Chemical Manufacturing and Accurate Detection, Key Laboratory of Chemical Sensing & Analysis in Universities of Shandong, School of Chemistry and Chemical Engineering, University of Jinan, Jinan 250022, P. R. China*

Xue Dong − *Collaborative Innovation Center for Green Chemical Manufacturing and Accurate Detection, Key Laboratory of Chemical Sensing & Analysis in Universities of Shandong, School of Chemistry and Chemical Engineering, University of Jinan, Jinan 250022, P. R. China*; orcid.org/0009-0001-9479-1979

Yujie Han − *Collaborative Innovation Center for Green Chemical Manufacturing and Accurate Detection, Key Laboratory of Chemical Sensing & Analysis in Universities of Shandong, School of Chemistry and Chemical Engineering, University of Jinan, Jinan 250022, P. R. China*

Huangxian Ju − *Collaborative Innovation Center for Green Chemical Manufacturing and Accurate Detection, Key Laboratory of Chemical Sensing & Analysis in Universities of Shandong, School of Chemistry and Chemical Engineering, University of Jinan, Jinan 250022, P. R. China; State Key Laboratory of Analytical Chemistry for Life Science, School of Chemistry and Chemical Engineering, Nanjing University, Nanjing 210023, P. R. China*; orcid.org/0000-0002-6741-5302

Complete contact information is available at: https://pubs.acs.org/10.1021/acs.analchem.5c07097

Notes

The authors declare no competing financial interest.

ACKNOWLEDGMENTS

This work was supported by the National Natural Science Foundation of China (22504042, 22206056, 22274062), the Natural Science Foundation of Shandong Province (ZR2022QB117), the Postdoctoral Innovation Program of Shandong Province (SDCX-ZG-202501031), and the Postdoctoral Fellowship Program of CPSF (GZC20250823).

REFERENCES

(1) Yao, L.; He, L.; Yang, Y.; Zhang, Y.; Liu, Z.; Liang, L.; Piao, Y. Nanobiochar paper based electrochemical biosensor for fast and ultrasensitive detection of microcystin-LR. *Sci. Total Environ.* **2021**, *750*, 141692.

(2) Bai, Z.; Wang, Z.; Wang, T.; Wu, Z.; Gao, X.; Bai, Y.; Wang, G.; Sun, K. Cation-vacancy engineering modulated perovskite oxide for

boosting electrocatalytic conversion of polysulfides. *Adv. Funct. Mater.* **2025**, *35* (14), 2419105.
(3) Luo, X.; Zhao, X.; Wallace, G. Q.; Brunet, M.-H.; Wilkinson, K. J.; Wu, P.; Cai, C.; Bazuin, C. G.; Masson, J.-F. Multiplexed SERS detection of microcystins with aptamer-driven core−satellite assemblies. *ACS Appl. Mater. Interfaces* **2021**, *13* (5), 6545−6556.
(4) Lv, L.; Chen, Q.; Jing, C.; Wang, X. An ultrasensitive ratiometric aptasensor based on the dual-potential electrochemiluminescence of $Ru(bpy)_3^{2+}$ in a novel ternary system for detection of Patulin in fruit products. *Food Chem.* **2023**, *415*, 135780.
(5) Song, X.; Wu, T.; Luo, C.; Zhao, L.; Ren, X.; Zhang, Y.; Wei, Q. Peptide-based electrochemiluminescence biosensors using silver nanoclusters as signal probes and Pd-Cu_2O hybrid nanoconcaves as coreactant promoters for immunoassays. *Anal. Chem.* **2021**, *93* (38), 13045−13053.
(6) Song, Y.; Tian, L.; Li, R.; Guo, Y.; Han, P.; Jiang, H.; Wang, W.; Wang, J. Electrochemiluminescence sensor based on resonance energy transfer for detection of chlortetracycline hydrochloride in food. *Food Chem.* **2025**, *483*, 144222.
(7) Shi, B.; Jia, Y.; Jia, D.; Tian, T.; Chen, J.; Ren, X.; Lei, J.; Jia, H.; Wang, H.; Wei, Q. Aggregation-induced electrochemiluminescence of $Ir(ppy)_3$-functionalized ZIF-8 for microcystin-LR detection via the trans-cleavage activity of CRISPR-Cas12a. *Anal. Chem.* **2024**, *96* (37), 15050−15058.
(8) Zhai, H.; Wang, Y.; Geng, L.; Guo, Q.; Zhang, Y.; Yang, Q.; Sun, X.; Guo, Y.; Zhang, Y. Bipotential-resolved electrochemiluminescence biosensor based on Bi_2S_3@Au nanoflowers for simultaneous detection of Cd(II) and ampicillin in aquatic products. *Food Chem.* **2023**, *414*, 135708.
(9) Du, Y.; Geng, H.; Chen, J.; Feng, R.; Wu, T.; Zhang, X.; Wei, Q. Supramolecular organic framework-enabled aggregation-enhanced electrochemiluminescence for ultrasensitive detection of MMP 9. *Anal. Chem.* **2025**, *97*, 21060−21070.
(10) Zhou, J.; Li, Y.; Wang, W.; Tan, X.; Lu, Z.; Han, H. Metal-organic frameworks-based sensitive electrochemiluminescence biosensing. *Biosens. Bioelectron.* **2020**, *164*, 112332.
(11) Zhang, C.; Lei, D.; Xie, C.; Hang, X.; He, C.; Jiang, H.-L. Piezo-Photocatalysis over Metal−Organic Frameworks: Promoting Photocatalytic Activity by Piezoelectric Effect. *Adv. Mater.* **2021**, *33* (51), 2106308.
(12) Wu, Q.; Liang, J.; Wang, D.; Wang, R.; Janiak, C. Host molecules inside metal−organic frameworks: host@MOF and guest@host@MOF (Matrjoschka) materials. *Chem. Soc. Rev.* **2025**, *54* (2), 601−622.
(13) Peng, L.; Xie, X.; Chen, X.; Chen, C. Electrochemical biosensors combined with nanomaterial signal amplification for the detection of alzheimer's disease biomarkers in blood. *ACS Sens.* **2025**, *10* (9), 6380−6405.
(14) Kirchon, A.; Feng, L.; Drake, H. F.; Joseph, E. A.; Zhou, H.-C. From fundamentals to applications: a toolbox for robust and multifunctional MOF materials. *Chem. Soc. Rev.* **2018**, *47* (23), 8611−8638.
(15) Zhu, D.; Zhang, Y.; Bao, S.; Wang, N.; Yu, S.; Luo, R.; Ma, J.; Ju, H.; Lei, J. Dual intrareticular oxidation of mixed-ligand metal−organic frameworks for stepwise electrochemiluminescence. *J. Am. Chem. Soc.* **2021**, *143* (8), 3049−3053.
(16) Bu, S.; Song, L.; Ding, Y.; Yang, Y.; Liang, Y.; Chai, Y.; Zhang, P.; Fu, Y.; Yuan, R. Dual-ligand ruthenium coordination polymer-derived self-enhanced electrochemiluminescent emitters for sensitive detection of procalcitonin. *Anal. Chem.* **2024**, *96* (26), 10809−10816.
(17) Qin, J.-S.; Yuan, S.; Wang, Q.; Alsalme, A.; Zhou, H.-C. Mixed-linker strategy for the construction of multifunctional metal−organic frameworks. *J. Mater. Chem. A* **2017**, *5* (9), 4280−4291.
(18) Sun, Q.; Qin, L.; Lai, C.; Liu, S.; Chen, W.; Xu, F.; Ma, D.; Li, Y.; Qian, S.; Chen, Z.; et al. Constructing functional metal-organic frameworks by ligand design for environmental applications. *J. Hazard. Mater.* **2023**, *447*, 130848.
(19) Wu, Y.; Xu, L.; Yang, J.; Hu, S.; Qin, D.; Deng, B. NiFe nanoalloy electrocatalyst as a coreaction accelerator for enhancing biomarker electrochemiluminescence imaging detection. *Anal. Chem.* **2024**, *96* (47), 18754−18763.
(20) Hu, L.; Wu, Y.; Xu, M.; Gu, W.; Zhu, C. Recent advances in co-reaction accelerators for sensitive electrochemiluminescence analysis. *Chem. Commun.* **2020**, *56* (75), 10989−10999.
(21) Gu, C.; Ji, S.; Chen, Z.; Yang, W.; Deng, Y.; Zhao, M.; Huang, W.; Yang, W.; Xu, W. Enrichment-catalytic synergistically enhanced electrochemiluminescence sensors based on IRMOF-3/CdTe for ultrasensitive detection of organophosphorus pesticides. *Biosens. Bioelectron.* **2025**, *279*, 117398.
(22) You, J.; Baktash, A.; Yao, D.; Zhang, Y.; Ding, S.; Hou, J.; Zhao, G.; Jin, Y.; Wang, Z.; Wang, L. Phase effect of TiO_2 on surface hydrogen adsorption/desorption in controlling photocatalytic methane conversion. *Chem. Sci.* **2025**, *16* (23), 10357−10363.
(23) Sampath, A.; Ricciardulli, T.; Priyadarshini, P.; Ghosh, R.; Adams, J. S.; Flaherty, D. W. Spectroscopic evidence for the involvement of interfacial sites in O−O bond activation over gold catalysts. *ACS Catal.* **2022**, *12* (15), 9549−9558.
(24) Huang, X.; Deng, X.; Deng, Z.; Wang, F. Bimodal electrochemiluminescence of Ru-MOFs in the presence of double coreactants for CEA detection. *Anal. Chem.* **2025**, *97* (23), 12207−12214.
(25) Hu, J.; Lao, H.-X.; Xu, X.-W.; Wang, W.-K.; Wang, L.-L.; Liu, Q.-Q. In situ meso-tetra (4-carboxyphenyl) porphyrin ligand substitution in Hf-MOF for enhanced catalytic activity and stability in photoredox reactions. *Rare Met.* **2024**, *43* (6), 2682−2694.
(26) Wang, L.; Song, L.; Yang, Z.; Chang, Y. M.; Hu, F.; Li, L.; Li, L.; Chen, H.-Y.; Peng, S. Electronic Modulation of Metal−Organic Frameworks by Interfacial Bridging for Efficient pH-Universal Hydrogen Evolution. *Adv. Funct. Mater.* **2023**, *33* (1), 2210322.
(27) Zhang, M.; Luo, K.; Fan, Y.; Lu, X.; Ye, J.; Lu, N.; Dong, J.; Niu, Q.; Zhang, J.; Zhang, P.; et al. Metal vacancies and self-reconstruction of high entropy metal borates to boost the oxygen evolution reaction. *Chem. Eng. J.* **2024**, *493*, 152758.
(28) Xiang, X.; Jing, J.; Wang, H.; Wang, X.; Li, M.; Wang, F.; Chen, J.; Guo, Y.; He, L.; Zhao, H.; et al. Synergistic a-site compensation and oxygen vacancy engineering boost high-entropy electrolyte performance in protonic ceramic fuel cells. *Nano Lett.* **2025**, *25* (21), 8464−8472.
(29) Zhong, W.; Yang, C.; Wu, J.; Xu, W.; Zhao, R.; Xiang, H.; Shen, K.; Zhang, Q.; Li, X. Oxygen vacancies induced by charge compensation tailoring Ni-doped Co_3O_4 nanoflakes for efficient hydrogen evolution. *Chem. Eng. J.* **2022**, *436*, 134813.
(30) Ren, R.; Wang, Z.; Meng, X.; Xu, C.; Qiao, J.; Sun, W.; Sun, K. Boosting the electrochemical performance of Fe-based layered double perovskite cathodes by Zn^{2+} doping for solid oxide fuel cells. *ACS Appl. Mater. Interfaces* **2020**, *12* (21), 23959−23967.
(31) Xiang, Y.; Liu, J.; Chen, Y.; Zhang, H.; Ren, L.; Ye, B.; Tan, W.; Andreas, K.; Hou, J. The change of coordination environments induced by vacancy defects in hematite leads to a contrasting difference between cation Pb(II) and oxyanion As(V) immobilization. *Environ. Pollut.* **2024**, *344*, 123318.
(32) Wang, X.; Zhu, L.; Lv, Z.; Qi, Z.; Xu, Y.; Miao, T.; Fu, X.; Li, L. Coupled visible-light driven photocatalytic reactions over porphyrin-based MOF materials. *Chem. Eng. J.* **2022**, *442*, 136186.
(33) Su, H.; Wang, W.; Jiang, H.; Sun, L.; Kong, T.; Lu, Z.; Tang, H.; Wang, L.; Liu, Q. Boosting interfacial charge transfer with a giant internal electric field in a TiO_2 hollow-sphere-based S-scheme heterojunction for efficient CO_2 photoreduction. *Inorg. Chem.* **2022**, *61* (34), 13608−13617.
(34) Lv, G.; Ye, H.; Lai, C.; Ma, D.; Zhou, X.; Huo, X.; Deng, H.; Tang, L.; Tong, T.; Yan, M.; et al. Ultrathin LDH-coated SnO_2 catalysts linked by hydrogen bonding for PMS activation via interlayer high-speed electron transfer channels: Performance and mechanism. *J. Environ. Chem. Eng.* **2025**, *13* (1), 115029.
(35) Oberhammer, H. Gas phase structures of peroxides: Experiments and computational problems. *ChemPhysChem* **2015**, *16* (2), 282−290.

https://doi.org/10.1021/acs.analchem.5c07097
Anal. Chem. 2026, 98, 6139−6148

(36) Xu, W.; Wu, Y.; Yu, X.; Wang, H.; Qin, Y.; Yang, W.; Hu, L.; Zheng, L.; Gu, W.; Lin, Y.; et al. Ru−OH−Zr site over metal−organic frameworks boosts coreactant activation for efficient electrochemiluminescence. *Nano Lett.* **2025**, *25* (1), 276−283.

https://doi.org/10.1021/acs.analchem.5c07097
Anal. Chem. 2026, 98, 6139−6148